Journal of Quantitative Spectroscopy & Radiative Transfer 324 (2024) 109063

Contents lists available at ScienceDirect

Journal of Quantitative Spectroscopy and Radiative Transfer

journal homepage: www.elsevier.com/locate/jqsrt

# On the impact of radiative transfer in fluorescence imaging of bacterial films and suspensions

Joshua M. Herzog *, Gianna Agosta, Volker Sick

*Department of Mechanical Engineering, University of Michigan, 2350 Hayward St., Ann Arbor, MI 48109, United States of America*

ARTICLE INFO

*Keywords:*
Monte Carlo
Fluorescence
Front-face spectroscopy
Scattering
Radiative Trapping
Bacterial biofilm

ABSTRACT

Fluorescence imaging and spectroscopy are convenient, rapid, and simple methods to analyze chemical samples including biological materials such as bacterial biofilms and suspensions. In principle, these techniques could be used to diagnose or discriminate between infectious bacteria in infections of the skin or ocular surface (*microbial keratitis*, MK). However, the extension of these techniques to macroscopic turbid media that strongly absorb and scatter light is difficult. Radiative transfer effects obscure the relationship between microscopic scattering and absorption properties and macroscopically observable quantities such as fluorescence intensity, transmission, and reflection. A combination of experimental measurements of aqueous bacteria cell suspensions and *Monte Carlo* radiation transfer simulations are performed to better understand these effects. Several general observations, *e.g.,* that fluorescence intensity is maximized in scattering-dominated media, are discussed in detail. It was found that wavelength-dependent radiative transfer effects are observable even at moderate optical densities (OD ~ 1; well below the diffusion limit). Careful consideration of radiative transfer effects using physically rigorous models is needed to determine single-cell scattering and absorption properties and interpret quantitative fluorescence measurements accurately in most cases of interest. A detailed discussion of radiative transfer effects and analytical models is provided. In the context of surface infections and MK, it was found that radiative transfer effects may be negligible for the model bacteria *E. coli* in some cases. However, more accurate measurements of microbe optical properties are needed to confirm and extend this conclusion to other species. Overall this work demonstrates that quantitative fluorescence imaging and spectroscopy of bacterial films and suspensions is feasible, but requires detailed sample characterization and careful consideration of radiative transfer effects.

## 1. Introduction

Fluorescence imaging and spectroscopy are powerful analytical chemistry techniques with diverse biomedical applications in chronic wound infections [1], tissue analysis [2], cancer detection [3,4], microbiology [5–8], and waste water monitoring [9]. The utility of fluorescence spectroscopy and imaging in these applications lies in the ability to uniquely target or discriminate between specific chemicals based on their ability to interact with light which in turn is related to molecular structure. For simple chemicals and systems, fluorescence imaging and spectroscopy can be used to discern detailed information about chemical structure, concentration, and thermodynamic state [10, ch. 11].

One particular application of interest is the detection and discrimination of surface infections, *e.g.*, those of the cornea (*microbial keratitis*, MK) for which standard diagnostic procedures often do not produce clinically useful results [11]. While fluorescence spectroscopy and imaging are believed to be capable detecting and discriminating between microbial species for this purpose [12], the impact of radiative transfer in fluorescence imaging and spectroscopy of optically-thick macroscopic biofilms such as MK infiltrates is unclear [13]. In particular, it is unclear whether fluorescence intensity can be used as an indicator of infiltrate thickness, and whether single-cell fluorescence spectra are representative of MK infiltrates.

Unlike in simple aerosols or solutions, most biological samples of interest are not optically thin or transparent. Variation in refractive index on the scale of the excitation or emission wavelength can cause elastic scattering leading to macroscopic radiative transfer effects [14]. These radiative transfer processes, which are particularly significant when photons undergo more than one interaction (multiple scattering), can alter the intensity of excitation light that reaches the fluorophore, or alter the transport of fluorescence emission from the sample, or both. And, since absorption and scattering are both wavelength-dependent

* Corresponding author.
*E-mail address:* jmherzog@umich.edu (J.M. Herzog).

https://doi.org/10.1016/j.jqsrt.2024.109063
Received 21 November 2023; Received in revised form 1 March 2024; Accepted 26 May 2024
Available online 27 May 2024

**Nomenclature**

| | |
|---|---|
| CMOS | Complementary metal-oxide semiconductor |
| HG | Henyey–Greenstein |
| HeNe | Helium–Neon |
| LED | Light-emitting diode |
| MC | *Monte Carlo* |
| MK | Microbial keratitis |
| OD | Optical density |
| RPM | Revolutions per minute |
| SBR | Signal-to-background ratio |
| SNR | Signal-to-noise ratio |
| UV | Ultraviolet |
| BL | Beer–Lambert |
| H | Chandrasekhar $H$-function |
| XY | Chandrasekhar $X$- and $Y$-functions |
| $\alpha$ | Single-scatterer albedo |
| $\lambda$ | Wavelength |
| $\mu$ | Direction-cosine |
| $\mu_0$ | Incident direction-cosine |
| $\Phi$ | Fluorescence quantum yield |
| $\sigma_a$ | Single-cell effective absorption cross-section |
| $\sigma_e$ | Single-cell effective extinction cross-section |
| $\sigma_s$ | Single-cell scattering cross-section |
| $\tau$ | Optical density |
| $\theta$ | Scattering angle |
| $g$ | Scattering anisotropy parameter |
| $I$ | Irradiance |
| $I_0$ | Incident irradiance |
| $I_r$ | Diffusely reflected irradiance |
| $I_t$ | Diffusely transmitted irradiance |
| $k_a$ | Biofilm absorption coefficient |
| $k_e$ | Biofilm extinction coefficient |
| $k_s$ | Biofilm scattering coefficient |
| $L$ | Sample length or thickness |
| $n$ | Number density |
| $N_0$ | Initial number of photon packets |
| $V_c$ | Bacteria cell volume |
| $A$ | Total absorbance |
| $F$ | Front-face fluorescence coefficient |
| $R$ | Total reflection coefficient |
| $R_D$ | Diffuse reflection coefficient |
| $R_S$ | Specular reflection coefficient |
| $T$ | Total transmission coefficient |
| $T_B$ | Ballistic transmission coefficient |
| $T_D$ | Diffuse transmission coefficient |
| $h_j$ | $j$th moment of Chandrasekhar's $H$-function |
| $x_j$ | $j$th moment of Chandrasekhar's $X$-function |
| $y_j$ | $j$th moment of Chandrasekhar's $Y$-function |
| $E_j(z)$ | $j$th-order generalized exponential integral function |
| $H(\mu)$ | Chandrasekhar's $H$-function |
| $X(\mu;\tau)$ | Chandrasekhar's $X$-function |
| $Y(\mu;\tau)$ | Chandrasekhar's $Y$-function |

processes, these effects impact the measured fluorescence or absorption spectrum. In imaging or spatially-resolved applications, multiple scattering additionally can delocalize light which in turn reduces spatial resolution, signal-to-noise ratio (SNR), and signal-to-background ratio (SBR).

One often seen radiative transfer effect is reabsorption of fluorescence emission, which is sometimes described as the "inner filter effect" since a portion of the fluorescence emission is reabsorbed or "filtered" as it exits a system giving the appearance of an additional filter on the collection optics. Reabsorption dominates when scattering processes are insignificant, *e.g.*, in optically thick solutions. Correction for reabsorption is conceptually straightforward and has been discussed in detail [15]. If there is significant overlap between the absorption and emission bands, the emission and absorption process can be repeated indefinitely leading to what is typically referred to as radiation trapping [16], a phenomenon that is conceptually similar to multiple scattering but is damped by nonradiative deactivation.

It seems to be generally accepted that exciting and collecting emitted radiation from the same face of the sample (*i.e.*, front-face or *en face* fluorescence spectroscopy) avoids high-concentration effects [17–19], but as will be shown here it is not generally possible to avoid these effects entirely. For bacterial biofilms and suspensions, as well as other samples that are scattering-dominated with trace fluorophore concentrations, there is added complexity from scattering which causes light transport in addition to attenuation that makes interpretation and correction of data difficult. This is true even for cases with only small amounts of scattering in solution [20]. The simplest analytical description of scattering comes from the Beer–Lambert law which states that all interactions (scattering and absorption events) remove photons or reduce the incident light intensity along the beam path. In reality, scattering events redirect light [21] providing additional opportunities for photons to be transmitted through or absorbed in a medium, altering the effective transmission and absorbance. Scattering also causes beam spreading, increased penetration depth, and other effects that limit spatial resolution and increase background. Anisotropy and sample size or geometry also influence fluorescence measurements, but their impact is more difficult to quantify.

In this work, a series of experiments and simulations were performed to investigate the impact of radiative transfer on *en face* fluorescence imaging of bacterial biofilms and suspensions. Analytical models of radiative transfer are also discussed and compared with the results. In addition to identifying the limits at which the Beer–Lambert law and linear approximations break down, this work aims to illustrate the influence of microscopic parameters (*e.g.*, albedo) on the observed, macroscopic fluorescence emission to aid in interpretation of experimental fluorescence data in future experiments.

## 2. Methods

Radiative transfer was studied experimentally in bacteria suspensions via dilution series using a custom two-color fluorescence imaging device described in detail in [12]. Radiative transfer was also studied in detail computationally using a series of *Monte Carlo* simulations for parameters believed to be representative of dense *E. coli* biofilms. Due to the nature of the radiative transfer equations (*i.e.,* no explicit scale dependence for most quantities), the MC results are largely also applicable to aqueous suspensions. However, for simplicity, the results will be discussed primarily in the context of a dense biofilm which is more relevant to clinical practice (*e.g.*, infections or ulcers on the skin or ocular surface).

Computational and experimental results are reconciled with analytical models to provide a means to interpret results and extrapolate for the design and optimization of diagnostic tools. Here we employ the theoretically rigorous Chandrasekhar solution [22] for the analytical solution. A more approximate approach often used in biomedical optics is the Kubelka–Munk (KM) theory [23]. However, the KM theory is less rigorous; in particular, the KM theory fails at high absorbances and the KM coefficients are not necessarily representative of the true particle absorption and scattering cross-sections [24,25]. Indeed, [24] makes a strong case for utilizing the Chandrasekhar theory in quantitative spectroscopy.

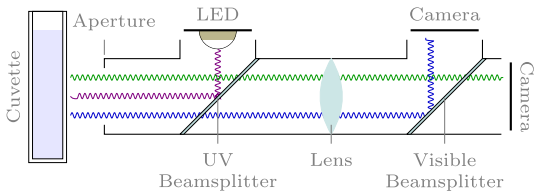


**Fig. 1.** Illustration of experimental setup showing cuvette with aqueous solution, imaging aperture, LED, beamsplitters and cameras.

### 2.1. Dilution series experiments

A dilution series was performed to evaluate the change in fluorescence intensity for a two-color line-of-sight imaging technique. The imaging technique was described previously in detail [12]. Here, the imaging system is used to illuminate and image fluorescence from aqueous suspensions of bacteria in UV-transparent rectangular cuvettes. Briefly, a collimated ultraviolet LED (ThorLabs M365LP1) source is directed onto the front-surface of the cuvette using a dichroic beamsplitter (Semrock FF389-Di01). Two nominally-identical scientific CMOS sensors (ThorLabs CS165MU1) share an achromatic lens (Edmund Optics #65–976) and UV-rejection filter (ThorLabs FELH0400) and are separated by a dichroic visible beamsplitter (Semrock FF458-Di02). Finally, each camera is outfitted with either a long- (Red band; ThorLabs FELH0450) or short-pass (Blue band; ThorLabs FESH0450) filter to further restrict the collection bands. A diagram illustrating the experimental setup is shown in Fig. 1.

Measurements were made of *E. coli* suspensions prepared from liquid nutrient broth cultures. Stock cultures of *E. coli* were purchased (Carolina Biological Supply) on nutrient agar. A small amount ($\sim$ 2 μL) of the culture was collected to inoculate 225 mL of nutrient broth (Edge Biologicals) in 500 mL sterilized flasks. The inoculated flasks were left at room temperature for two weeks until significant growth was observed, and measurements were repeated over approximately one month.

For each measurement, 2 mL of culture was collected with a sterilized pipette and placed into a UV-transparent disposable cuvette to estimate cell concentration. Concentration was determined using elastic scattering imaging with a Helium-Neon (HeNe) laser (Melles Griot 05-LLR-811) and scientific CMOS camera (LaVision Imager sCMOS) with 50 mm $f/1.4$ lens (Nikon Nikkor MF $f/1.4$). Elastic scattering intensity along the beam centerline was fit to an exponential model to estimate OD as $\mathrm{OD} = -\ln I(L)/I(0)$.

An additional 6 mL of culture was then collected and washed to remove nutrient broth that would otherwise interfere with the fluorescence imaging measurement. The total of 8 mL of broth was centrifuged at 5000 RPM for 5 min to remove cells from the suspension. The cells were then rinsed with distilled water and centrifuged again at 5000 RPM for 5 min. The rinsed cells were then re-suspended in 3 mL distilled water in a sterilized UV-transparent rectangular cuvette.

The fluorescence imaging procedure was performed directly on the cuvettes containing the aqueous cell suspension. After imaging of the initial suspension, 0.5 mL of the suspension is removed from the cuvette and replaced with an equal amount of distilled water and mixed thoroughly, and the imaging procedure is repeated. This procedure corresponds to a dilution factor of $5/6$ per iteration. The dilution was repeated 15 to 20 times until no further significant change in fluorescence intensity was observed. A background image pair was taken with the LED off for each iteration, and a fluorescence image pair was taken of a reference target for each experiment for image correction. After background subtraction and flatfield correction, the images were cropped to a circle of approximately 3 mm diameter at the center of the cuvette for analysis to minimize bias from the cuvette walls. Fluorescence intensities were calculated for each image band and concentration, and fit to a double exponential formula. The zero concentration component of the fit is taken to be the cuvette wall fluorescence and is subtracted before further analysis.

OD was measured once via laser extinction and subsequent values were calculated based on the dilution factor such that the reported OD value is proportional to cell concentration. This approach was selected since OD based on laser extinction is not necessarily proportional to concentration in highly scattering media, as illustrated by this and related work. The actual OD is expected to be larger than the measured value due to strong forward-scattering, but no further attempt was made to correct the OD value. The precision of the relative OD value following dilution is approximately 4% based on 15 repeated dilutions with a ~1% repeatability based on half of the minimum pipette graduation, and the bias limit is ~8% based on pipette tolerance. The total relative OD accuracy is therefore ~10%.

### 2.2. Monte Carlo simulations

*Monte Carlo* radiative transfer simulations were run using a custom code. A detailed overview of *Monte Carlo* methods for light transport is given in [26], and a review of recent advances and applications is given by [27]. Briefly, for each simulation, an initial group of $N_0$ photon packets are generated that are normally-incident on an infinite slab of thickness $L$ and allowed to propagate stochastically through the medium.

For the current work, the cell number density $n$ is held constant at $n = V_c^{-1}/2 \approx 5 \times 10^8$ mm$^{-1}$ where $V_c = 1$ μm$^3$ is an order of magnitude cell volume estimate for *E. coli*. The scattering cross-section $\sigma_s$ is also held constant at 1 μm$^2$ which is representative of *E. coli* at near-UV wavelengths [28] and is consistent with Mie scattering calculations using spherical-equivalent volumes [29]. Typical infiltrates in MK are on the order of 0.1 mm thick [30], corresponding to optical densities on the order of 10 to 100.

The effective absorption cross-section $\sigma_a$ is varied for each simulated condition. Scattering anisotropy is implemented using the Henyey–Greenstein (HG) phase function [31] with fixed anisotropy parameter $g = 0.98$ based on Mie scattering using the spherical-equivalent cell volume of *E. coli* cells in water (or extracellular matrix) for light of wavelength $\lambda = 370$ nm. The computational domain is a cylinder of radius 1 mm with a refractive index of 1.33, while the front, back, and side surfaces have a refractive index of 1.6; this is representative of water or a biofilm surrounded by glass with an index-matched immersion oil for the collection optics. A pencil beam of photon packets are initially normally-incident on the slab along the cylinder axis. Reflections are assumed to be specular with a transmission probability determined by the Fresnel reflection equations. The Fresnel reflection coefficient for the interface is $R_S \approx 0.0085$ at normal incidence, which is largely negligible but may have a small impact on, *e.g.*, diffuse reflectance.

Simulations are run in quasi-static "single-photon" mode, in which each packet is treated as a single particle that is either transmitted, scattered, or absorbed as a whole. Fluorescence is generated at the same location following absorption events to avoid spatial sampling bias. Absorption, transmission, and reflection coefficients are calculated as the fraction of photons that are absorbed, transmitted, or reflected, respectively. The fluorescence coefficient is calculated as the number of fluorescence photons that escape through the front surface divided by the number of incident photons. The fluorescence quantum yield ($\Phi$) is chosen to be unity for simplicity. The simulation parameters are summarized in Table 1. Based on the number of photon packets, the detection limits are $N_0^{-1} = 2 \times 10^{-7}$. An illustration of the assumed geometry and radiometric quantities is shown in Fig. 2.

Uncertainty in the radiometric measurements including reflection, transmission, and fluorescence intensities is estimated as the coefficient

**Table 1**
Parameter ranges for *Monte Carlo* radiative transfer simulations.

| Parameter | Symbol | Values | Unit |
|---|---|---|---|
| Initial packets | $N_0$ | $5 \times 10^6$ | – |
| Scattering anisotropy | $g$ | 0.98 | – |
| Cell density | $n$ | $5 \times 10^8$ | $mm^{-3}$ |
| Wall refractive index | $m_w$ | 1.6 | – |
| Medium refractive index | $m$ | 1.33 | – |
| Film geometry | – | Cylindrical | – |
| Film radius | $R$ | 1 | mm |
| Film thickness | $L$ | $10^0$–$10^4$ | μm |
| Scattering Cross-section | $\sigma_s$ | 1.0 | $\mu m^2$ |
| Absorption Cross-section | $\sigma_a$ | 0–$10^3$ | $\mu m^2$ |
| Scattering OD | $OD_s$ | $5 \times 10^{-1}$–$5 \times 10^3$ | – |

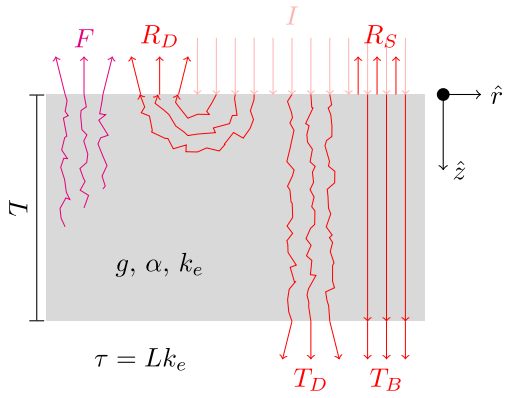


**Fig. 2.** Illustration of slab geometry with incident rays $I$ from above, ballistic and diffuse transmission $T_B$ and $T_D$, specular and diffuse reflection $R_S$ and $R_D$, and fluorescence emission from top (incident) surface $F$. The slab has a thickness $L$, extinction coefficient $k_e$, scattering anisotropy $g$, albedo $\alpha$, and optical thickness $\tau$ as illustrated.

of variation (COV) based on Poisson statistics, and was verified by repeating several simulations. The COV is calculated as

$$\frac{\sigma_x}{\mu_x} = \frac{1}{\sqrt{N_0 x}} \tag{1}$$

Where $\sigma_x/\mu_x$ is the COV or fractional uncertainty in the measured intensity $x$, and $N_0$ is the number of photon packets in the simulation. The product $N_0 x$ is thus the number of measured photon packets. For the radiometric quantities presented here ($R$, $A$, $T$, $F$), the COV is 0.4 and 0.1 for $x \approx 10^{-6}$ and $x \approx 10^{-5}$, respectively. The uncertainty in penetration depth is negligible $\sigma_\delta/\mu_\delta \approx 10^{-3}$ as every packet contributes to the calculation.

### 2.3. Analytical modeling

Analytical descriptions of radiative transfer processes are based on the theory derived by Chandrasekhar [22] for isotropic scattering in plane scattering media (see ch. 3 and 5 of [22] for a detailed derivation of isotropic and anisotropic diffuse reflectance, respectively). Briefly, the transmission, absorption, and reflection coefficients of a finite layer of material are constructed in terms of the solutions $X$ and $Y$ to a set of integral equations. The expressions for reflected irradiance $I_r$ and transmitted irradiance $I_t$ are

$$I_r(\mu, \mu_0) = I_0(\mu_0)\frac{\alpha}{4}\frac{\mu_0}{\mu + \mu_0}\left[X(\mu)X(\mu_0) - Y(\mu)Y(\mu_0)\right] \tag{2a}$$

and

$$I_t(\mu, \mu_0) = I_0(\mu_0)\frac{\alpha}{4}\frac{\mu_0}{\mu - \mu_0}\left[Y(\mu)X(\mu_0) - X(\mu)Y(\mu_0)\right] \tag{2b}$$

where $\mu_0$ is the cosine of the incident angle relative to the surface normal (for simplicity, here we only consider the case of $\mu_0 = 1$), $\mu$ is the direction cosine of the transmitted or reflected light, and $\alpha = k_s/(k_s + k_a)$ is the single-scatterer albedo. The solutions $X$ and $Y$ are functions of a direction cosine $0 \le \mu \le 1$, and implicitly depend on optical thickness $\tau$, albedo $\alpha$, and the scattering phase function. Total diffuse reflectance and transmittance requires integrating $I_r$ and $I_t$ over solid angle giving

$$R_D = 1 - (1 - x_0)X(\mu_0) - y_0 Y(\mu_0) \tag{3a}$$

and

$$T_D = (1 - x_0)Y(\mu_0) + y_0 X(\mu_0) - e^{-\tau/\mu_0} \tag{3b}$$

while the ballistic and total transmittances are

$$T_B = e^{-\tau/\mu_0}, \tag{3c}$$

and

$$T = T_D + T_B, \tag{3d}$$

and absorbance is calculated as

$$A = 1 - R_D - T_D - T_B. \tag{3e}$$

where $x_0$ and $y_0$ are the zeroth moments of the $X$ and $Y$ functions at the specified optical density $\tau$. The integrals are evaluated numerically during the calculation of $X$ and $Y$. The penetration depth into the medium is estimated as the weighted average of intensity over optical depth $\tau$, or

$$\delta = \frac{\int_0^\tau T\ \tau'\ d\tau'}{\int_0^\tau T\ d\tau'} \tag{4}$$

To calculate fluorescence intensity, we estimate the amount of fluorescence light emitted in an infinitesimal slice of width $d\tau'$ as $dF_e = \Phi dA = \Phi\ \partial A/\partial\tau'\ d\tau'$. The fraction of this infinitesimal fluorescence that is detected exiting the film at $\tau = 0$ is given by the transmission coefficient for a layer of optical thickness $\tau'$ such that $dF = dF_e\ T = dF_e\ [y_0 X(\mu) + (1 - x_0)Y(\mu)]d\tau'$. Integrating over the layer thickness and exit angle $\mu$ (assuming the emission is isotropic) results in

$$F(\tau) = \Phi \int_0^\tau \left.\frac{\partial A}{\partial \tau}\right|_{\tau'} \left(y_0 x_1 + (1 - x_0)y_1\right) d\tau', \tag{5}$$

where $x_1$ and $y_1$ are the first moments of the $X$ and $Y$ functions, and the integral over $\tau'$ is evaluated numerically. For the case of isotropic scattering for small values of $\alpha\tau$, an analytical expression can be derived (see Appendix) as

$$F(\tau) \approx \Phi(1 - \alpha)\frac{\alpha^2}{16}\left(1 - 2e^{-\tau}E_3(\tau)\right), \tag{6}$$

where $E_j(z)$ is the generalized exponential integral function of order $j$. This approximation demonstrates several features that will be discussed further in Section 4.

Chandrasekhar's theory can additionally be extended to anisotropic scatterers by including an appropriate phase function in the kernel of the integral equations for $X$ and $Y$. Most cases of interest are strongly anisotropic, such as bacteria cells at visible wavelengths in liquid suspension or in air, but direct calculation of $H$, $X$ and $Y$ in this manner is difficult and computationally intensive. A detailed discussion regarding the difficulty in solving the radiative transfer equation is provided in [32]. Instead, we approximate anisotropy using similarity rules for radiative transfer [33] such that $H$, $X$, and $Y$ do not need to be reevaluated for every new cell geometry. The reduced scattering coefficient, reduced albedo, reduced extinction coefficient, and reduced optical density are defined as

$$k_s' = k_s(1 - g) \tag{7a}$$

$$k'_e = k'_s + k_a = k_e(1 - \alpha g), \tag{7b}$$

and therefore

$$\alpha' = \frac{k'_s}{k'_e} = \alpha \frac{1-g}{1-\alpha g}, \tag{7c}$$

and finally

$$\tau' = \tau(1 - \alpha g) \tag{7d}$$

where $g$ is the scattering anisotropy parameter (the average change in $\mu$ for a single scattering event). Using these definitions, we approximate anisotropic behaviors in biofilms by taking $\alpha \to \alpha'$ and $\tau \to \tau'$ in Eqs. (3).

Finally, the beam spread function or radius at the back surface of the film provides a useful measure of diffusion and beam broadening. Beam spread is difficult to quantify within Chandrasekhar's theory since the theory is implicitly one-dimensional. Instead, Van de Hulst [34] derived an exact analytical beam spread function for strongly forward-scattering media. Van de Hulst's solution can be contracted to show that, at depth $z$ along centerline and at a perpendicular radius $r$ from the centerline, the irradiance of a beam broadened by a forward-scattering medium is

$$I(r,z) = \sqrt{\frac{3}{2\pi k'_s z^3}} e^{-\frac{3}{2}\frac{r^2}{k'_s z^3}} \tag{8}$$

such that the Gaussian beam radius at optical depth $\tau$ is

$$\sigma_R^2 = \frac{L^3 k'_s}{3} = \frac{1}{3}\frac{\alpha^3 \tau^3 (1-g)}{k_s^2} + \sigma_{R,0}^2 \tag{9}$$

where $L$ is the film thickness and $\sigma_{R,0}$ is the initial incident beam radius ($\sigma_{R,0} = 0$ in the MC results here). It is worth noting that Van de Hulst's theory is only valid if the second moment of the scattering phase function exists, which is not true for the HG function used here, so some deviation is expected compared with the *Monte Carlo* results. From our data, we find better agreement using Eq. (9) with $g \to 0$. We also note that due to the presence of absorption, the beam cannot spread beyond the limiting penetration depth which provides a limiting radius as

$$\sigma_{R,\infty} \approx \delta_\infty \langle \cos\theta \rangle \approx \delta_\infty g \tag{10}$$

where the subscript $\infty$ indicates the limit that $\tau \to \infty$ and $\theta$ is the average beam spreading angle due to scattering. The substitution of $g$ for $\langle \cos\theta \rangle$ is only possible for strongly-forward scattering media ($g \approx 1$).

## 3. Results

Results for dilution series experiments and *Monte Carlo* radiative transfer simulations are presented in the following sections.

### 3.1. Dilution series

Measurements of fluorescence intensity in both channels of the imaging system for a representative case are shown in Fig. 3. Three features are evident in the plot. First, fluorescence intensity in both channels is strongly nonlinear in concentration as expected. Second, the blue band response deviates from that of the red band, which is perhaps unsurprising given that *E. coli* attenuates blue wavelengths more strongly [5]. This does, however, contradict the assertion that *en face* imaging and spectroscopy is not strongly impacted by reabsorption. Finally, the response is described well by a double exponential model which was intuitively selected to describe Beer–Lambert like attenuation of the incident and emitted radiation.

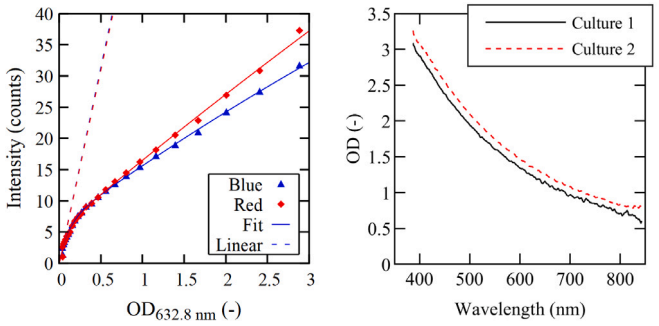


(a) Fluorescence intensity (b) Extinction spectra

**Fig. 3.** Measured fluorescence intensity of an aqueous *E. coli* suspension with varying concentration, and extinction spectra of two primary *E. coli* cultures over a 1 cm path length. Here, OD is calculate as $-\ln T$ for simplicity.

### 3.2. Monte Carlo simulations

Calculated transmission, absorption, reflection and fluorescence coefficients for the anisotropic (HG, $g = 0.98$) case are plotted in Figs. 4a–4d, and the corresponding penetration depth and exiting beam radius are shown in Figs. 4e–4f. For all cases, "Optical Density" refers to the quantity OD $= \tau = (\sigma_a + \sigma_s)nL$ and not the effective optical density, and the colorbar indicates the ratio of single-particle absorption to scattering $k_a/k_s = \sigma_a/\sigma_s$. In each plot, the shaded region indicates optical densities that are less than 10 cell diameters thick as a practical lower limit on biofilm thickness.

Four results are displayed. The *Monte Carlo* results are referred to using the label MC. The Chandrasekhar theory (Eq. (3)) is referred to using the label XY. A more computationally tractable semi-infinite slab solution for $\tau \to \infty$ based on Chandrasekhar's H-function is used as a limiting case and is labeled H. Finally, a simplified Beer–Lambert solution,

$$T = e^{-\tau} \tag{11a}$$

$$A = \alpha(1 - e^{-\tau}) \tag{11b}$$

is given the label BL. All of the models (XY, BL, and H) use the reduced albedo $\alpha'$ and optical density $\tau'$ to approximate anisotropy (Eq. (7)), while the MC results handle anisotropy exactly via the HG phase-function.

In all cases, the MC data matches well with the XY solution. Disagreement in reflection coefficient at small values of $\tau$ are a result of specular reflection from the substrate in the MC simulation which is not accounted for in the other calculations, but could be included with little additional effort. Disagreement in reflection coefficient at larger $\tau$ values and intermediate values of $\alpha$ is caused by anisotropy that is not captured exactly using the assumed similarity rules; this disagreement vanishes when $g = 0$.

Disagreement in the fluorescence coefficient between the XY and MC data is caused by three sources. The most significant source of error is likely the similarity rules since, similar to diffuse reflection, higher-order scattering events can contribute significantly to the end result especially for $\alpha \to 1$. Second, the MC simulation domain is finite in the radial direction which limits the acceptance angle for photon packets exiting the front surface of the simulation. Finally, specular reflections from the boundaries of the simulation domain, which are not accounted for in the analytical models, may also contribute.

In the simulation results presented so far, the absorption coefficient and albedo are identical for the incident and emitted radiation which likely is not accurate in practice, especially since $\sigma_s$ can vary strongly with scattering parameter $x$ near $x \approx 1$ and $\sigma_a$ can be strongly wavelength dependent based on chemical composition. An additional

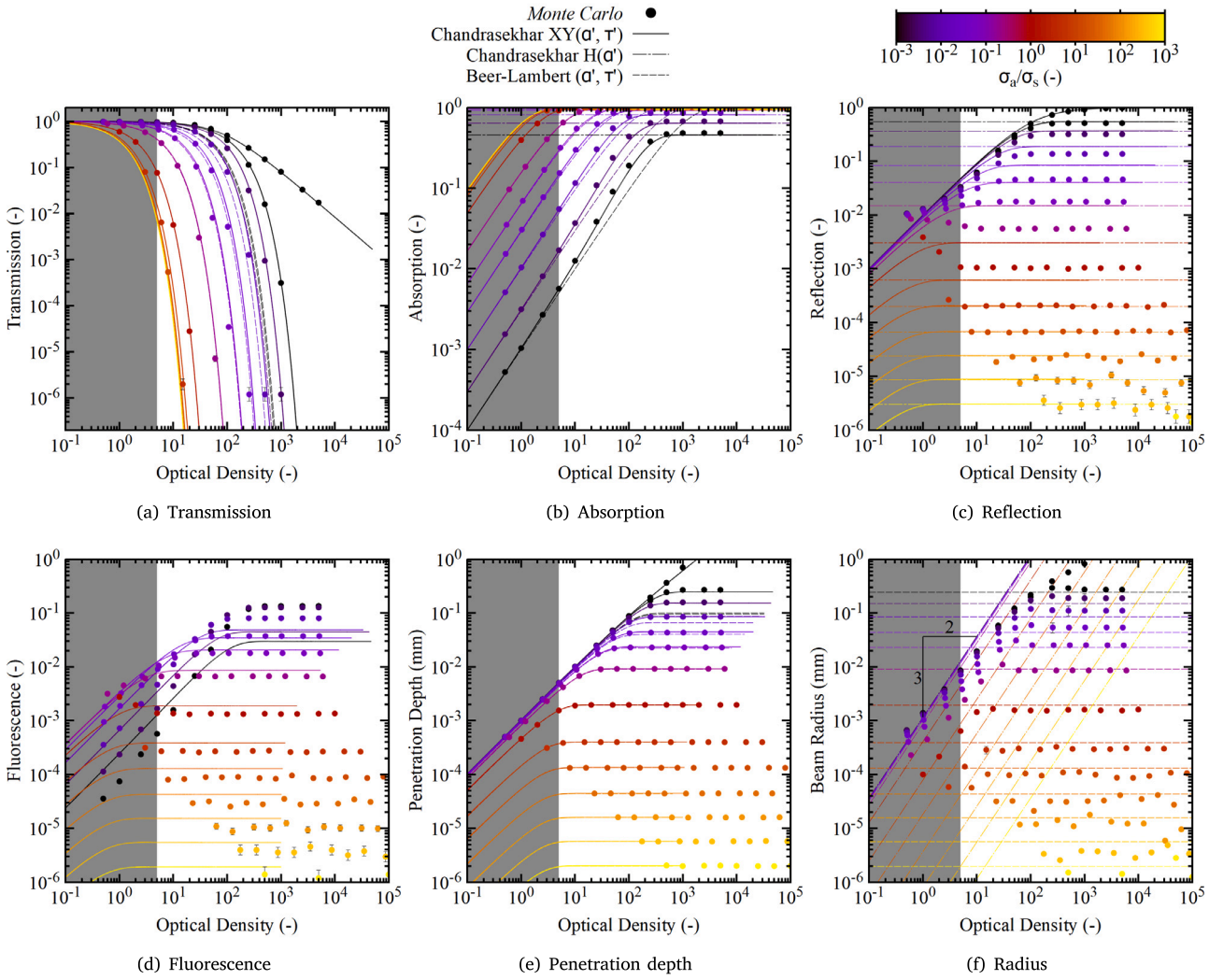


**Fig. 4.** *Monte Carlo* results. The shaded region in each plot indicates $L < 10$ μm, which is used here as an approximate lower bound on realistic biofilm thickness. Errorbars indicate one standard-deviation based on Poisson statistics, but in most cases are smaller than the marker size. In (f), the additional dashed lines with slope 2/3 indicate van de Hulst's solution calculated using $g = 0$.

set of simulations was run for three different absorption coefficients ($\sigma_a = 0.1$, 1, and 10 μm$^2$) for the incident radiation field, with varying absorption coefficient for the emitted fluorescence radiation ($\sigma_{a,e}$) specified by $\beta = \sigma_{a,e}/\sigma_a$. The fluorescence coefficients for these cases are plotted in Fig. 5. Wall reflections were disabled in this case to avoid misinterpretation. Two reference lines are superimposed on the plot. One line with slope 1 is drawn to illustrate collapse to the linear limit as $\tau \to 0$. The second line has slope 1/3 (corresponding to $F \propto \tau^{1/3}$) to illustrate the deviation of the results from the linear response at moderate values of $\tau$; in particular, the slope of 1/3 matches the MC results well for $\sigma_a = 0.1$ μm$^2$ and $\beta \to 0$.

Finally, an additional set of simulations was performed with varying anisotropy parameter $g$ for a semi-infinite film to assess the quality of the similarity scaling. For these cases, the diffuse reflectance is calculated in the MC simulation, and the effective albedo is chosen to be $\alpha'$ such that $R_{D,H}(\alpha') = R_{D,MC}(\alpha; g)$ where $R_{D,H}$ is the isotropic, semi-infinite slab diffuse reflectance calculated from Chandrasekhar's $H$-function. The calculated effective albedo, $\alpha'$, is plotted in Fig. 6 as a function of the reduced single-scatterer albedo $\alpha(1-g)/(1-\alpha g)$. From the plot, the similarity scaling produces the correct general trend but order of magnitude deviations occur at $g > 0$ and $\alpha < 1$. Based on the simulation data, the expression

$$\alpha' = \alpha \frac{1-g}{1-\alpha g} e^{-\frac{(1-\alpha)g}{1-\alpha g}} \tag{12}$$

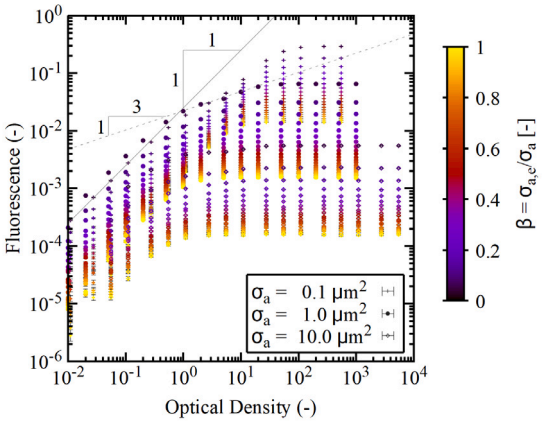


**Fig. 5.** Simulated fluorescence coefficient with $g = 0.98$, $\sigma_s = 1$ μm$^2$, and $\alpha = 0.091$, 0.5, and 0.91 for incident radiation, and $\sigma_{a,e} = \beta\sigma_a$ for fluorescence emission for a biofilm of varying thickness.

matches within 20% over the simulation domain and more typically within a few percent.

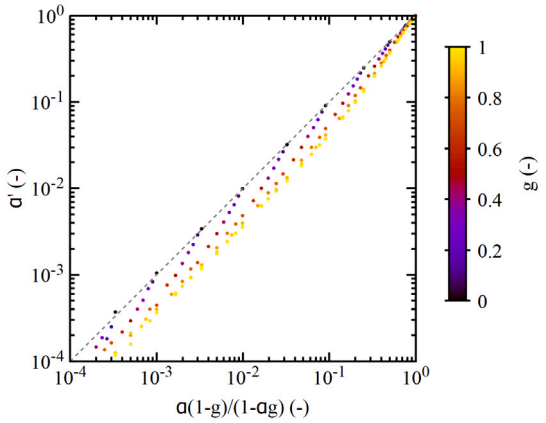


**Fig. 6.** Effective albedo based on diffuse reflectance for the HG phase function for a range of single-scatterer albedo $\alpha$ and anisotropy values $g$.

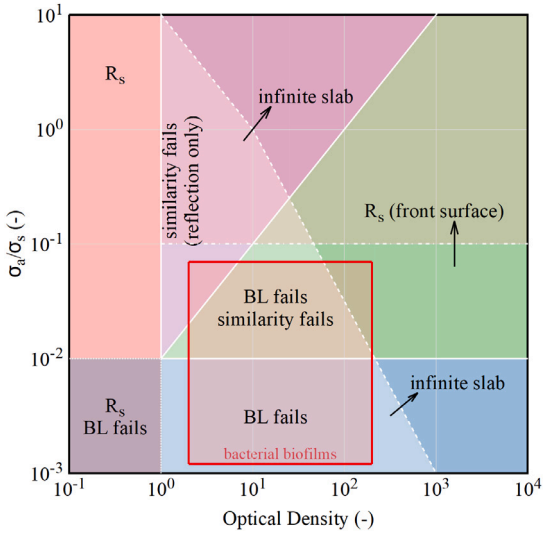


**Fig. 7.** Illustration of various complications identified in the interpretation of radiometric data as a function of sample OD and $\sigma_a/\sigma_s$ for strongly forward-scattering media (HG phase function with $g = 0.98$. The abbreviation $R_s$ indicates that specular reflections (from both front and back surfaces unless otherwise specified) are significant. Boundaries between regions are estimates and should not be interpreted quantitatively.

## 4. Discussion

Overall, the results demonstrate that radiative transfer effects (reabsorption, radiation trapping, and/or multiple scattering) are significant in *en face* fluorescence imaging of aqueous bacteria suspensions and films. Notably, the dilution series fluorescence intensity measurements continue to increase with increasing concentration throughout the range of concentrations under investigation, rather than approach a limiting value as might be expected. Further, at OD > 1 the blue and red band intensities diverge suggesting that wavelength-dependent radiative transfer effects are significant. In the data presented in Fig. 3(a), the ratio of the blue to red fluorescence intensity changes by more than 10% throughout the measured range.

There are also several features that are evident in the simulation results that are not necessarily intuitive. First, and perhaps most obvious, is that fluorescence intensity does not increase monotonically with $1 - \alpha = \sigma_a/\sigma_e$ at a given value of $\tau$. Rather, the cases which exhibit the largest fluorescence coefficients are scattering-dominated ($\alpha > 0.5$). Specifically, the maximum fluorescence coefficient observed in the MC simulations (for $\tau \to \infty$) occurs at $\sigma_a/\sigma_s = 10^{-3}$, which is the smallest non-zero absorption coefficient used. Similar behaviors were observed for the isotropic scattering case, albeit with slightly reduced peak albedo values. The solution via the Chandrasekhar $X$ and $Y$ functions in the isotropic case peak at $\alpha \approx 2/3$ which is consistent with the first-order analytical approximation for $F$ (Eq. (6)) which is maximized at $\alpha = 2/3$. Put another way, the fluorescence intensity depends strongly on (wavelength-dependent) properties including albedo and scattering anisotropy even for very thick slabs.

One consequence of these behaviors is that line-of-sight fluorescence intensity is proportional to absorption cross-section only for predominantly scattering media. This is advantageous for fluorescence imaging or analysis of biofilms which typically have $\alpha \approx 1$. Fluorescence intensity of thick slabs measured in this way can be used as an indicator of single-cell fluorescence intensity (*i.e.*, $F \propto \Phi\sigma_a$) for fixed $\tau$.

Second, fluorescence intensity is only proportional to concentration (or optical density) in cases where $(1 - \alpha)\tau \lesssim 10^{-1}$, or more conservatively for $\tau < 10^{-1}$. This approximate cutoff can be observed in the MC data in Fig. 5, and in the dilution series results in Fig. 3(a). Above this threshold there is still significant increase in fluorescence intensity with increasing concentration or optical density but the slope is dependent on scattering and absorption characteristics. The dilution series data appears to scale in proportion to $\sqrt{\tau}$ for $\tau \gtrsim 0.1$, which is comparable to the high-albedo simulation results (*e.g.*, $\sigma_a = 0.1$ μm$^2$ and $\beta \ll 1$). In the MC results, the fluorescence coefficient eventually saturates. The onset of this "saturation regime" is dependent on the single-cell absorption and scattering characteristics. Since we expect $\tau > 1$ for typical biofilms, fluorescence intensity is generally not a good indicator of film thickness.

Third, the similarity scaling for anisotropy works well for $\alpha \to 1$, but results deviate significantly at smaller values of $\alpha$. For cases with non-negligible absorption, other methods are needed to account for anisotropy. A more accurate formula to estimate the effective albedo was presented; however, it is not clear how accurate this formulation would be in practice and it is beyond the scope of this work to evaluate alternative methods to account for scattering anisotropy.

Finally, the MC and XY results diverge significantly from the BL approximation. For transmission and absorption, the BL approximation incorrectly assumes that scattered light is removed from the beam. Forward-scattered photons have additional opportunities to be absorbed by a cell or to be transmitted, thus the BL approximation underestimates transmission significantly as $\alpha \to 1$, and absorption prior to saturation. It is particularly interesting to note in Fig. 4b a slight increase in absorption relative to the BL curve at moderate optical densities (*e.g.*, $k_a/k_s = 10^{-3}$ and $\tau \approx 10^2$).

### 4.1. Experimental considerations

Solution of the inverse problem, *i.e.*, estimating absorption and scattering cross-sections and concentrations from bulk fluorescence, reflection, or transmission data is clearly not straightforward in many cases. As demonstrated here, scattering can strongly impact transmission, reflection, fluorescence, and absorption differently depending on the regime. Generally speaking, the XY analysis here is sufficient to accurately describe diffuse transmission and absorption at all conditions investigated. Diffuse reflectance and fluorescence intensity are captured well qualitatively, but quantitative predictions fail at a wide range of conditions largely due to anisotropy that is not fully captured using the similarity scaling. This suggests that several additional factors need to be accounted for when interpreting and fitting data. A variety of complications in interpreting measurements were identified here, and are summarized graphically in Fig. 7 which codes regions of OD and $\sigma_a/\sigma_s$ according to failures in common assumptions. Note that the boundaries between regions are estimates that should not be interpreted quantitatively.

To summarize Fig. 7, the dominant source of error at low OD is specular reflections from both the front surface and back surface of the domain; this influences primarily diffuse reflectance and fluorescence measurements. At high OD the infinite slab limit becomes a useful approximation. For highly scattering cases with $\sigma_a/\sigma_s \lessapprox 10^{-2}$, the Beer–Lambert law fails to describe transmission and absorption due to the erroneous assumption that scattered light is removed from the beam. Conversely, highly absorbing cases can be described well with the Beer–Lambert law, but the similarity scaling fails and more precise methods are needed to account for scattering anisotropy. Specular reflections become significant for any cases where the diffuse reflection is small, namely those in which $\sigma_a/\sigma_s \gtrapprox 10^{-1}$. Considering the fluorescence emission specifically, we find that none of the theories presented are able to describe the MC results quantitatively, although the XY solution (using similarity scaling) is qualitatively correct. Bacterial suspensions and films are expected to be in an intermediate regime as marked in Fig. 7 which suggests that the Beer–Lambert law is likely insufficient to interpret data and that similarity scaling is insufficient to account for scattering anisotropy. It is clearly necessary to find improved methods to account for anisotropy and other factors to define the relationship between fluorescence intensity, diffuse reflection, and concentration. In all cases, it is imperative to ensure that additional factors specific to the experiment are accounted for. *E.g.*, for integrating sphere measurements without index-matching, internal reflections will likely be significant; for imaging, angular distributions for fluorescence and reflection can vary at low OD, so the collection solid-angle needs to be considered.

Altogether, the results presented here illustrate the complexity of quantitative radiometric measurements in turbid media such as bacterial films and suspensions. Given that typical bacteria cells are on the order of 1 μm in diameter, are optically soft in aqueous suspensions (and presumably biofilms), and fluoresce weakly, most measurements of interest likely fall into the intermediate $\tau$ regime (*i.e.*, below the infinite slab limit) with high albedo ($0.9 \lesssim \alpha < 1$) and strong forward-scattering ($0.5 \lesssim g < 1$). In this regime, most simple approximations of fluorescence coefficient fail, making analysis difficult. *En face* fluorescence imaging and spectroscopy of biofilms and suspensions require careful consideration of the relative contributions of scattering and absorption on the measurement.

### 4.2. Application to MK infiltrates

Regarding the application of fluorescence imaging and spectroscopy for detection of MK, it appears that radiative transfer effects may be negligible in thinner infiltrates but may become significant towards the upper end of the expected optical density range for MK infiltrates ($\tau \approx 10^2$). Assuming a fluorescence coefficient of 0.05 $mm^{-1}$ from [5], a cell volume of 1 $\mu m^3$, and $\Phi \approx 0.02$ based on NADH in water [35], an approximate per cell absorption cross-section can be estimated as $\sigma_a \approx 0.003$ $\mu m^2$, giving $k_a/k_s \approx 0.003$ and $\alpha \approx 0.997$ at 370 nm excitation. At these conditions, the fluorescence intensity and absorption fractions remain linear with $\tau$ below $\tau \approx 10^2$. However, scattering and absorption properties are expected to vary with species significantly; future work will be needed to more accurately identify typical optical densities, scattering cross-sections, and effective absorption cross-sections of microbial species of interest to verify this result for specific species.

## 5. Conclusion

Fluorescence imaging and spectroscopy are powerful analytical chemistry techniques that can offer detailed chemical information in a variety of disciplines including the biomedical sciences and applications in microbiology. Microbial cells are known to fluoresce appreciably, and previous studies have shown that this intrinsic fluorescence can in principle be used to diagnose, *e.g.*, infections of the cornea (*microbial keratitis*). However, small particle sizes on the order of the wavelength of light cause significant scattering leading to complicated macroscopic radiative transfer effects in condensed samples such as bacterial biofilms and suspensions. In this work, *E. coli* cell suspensions were analyzed experimentally, and a series of *Monte Carlo* radiative transfer simulations were run to improve our understanding of radiative transfer in bacterial biofilms and suspensions, particularly through the lens of fluorescence imaging and spectroscopy. It was found that physically rigorous methods to account for radiative transfer are needed to interpret *en face* fluorescence data even qualitatively, but transmission and absorption can be described accurately using similarity scaling. Fluorescence intensity was found to have a non-linear and non-monotonic dependence on albedo such that fluorescence intensity peaks in particle suspensions and films that are scattering dominated (albedo > 0.5). It was also observed that, in the absence of surface reflections and quenching, fluorescence intensity is a monotonically non-decreasing function of concentration or film thickness. However, empirical measurements of effective optical density and albedo may be sufficient. In the context of *microbial keratitis*, our results suggest that fluorescence spectroscopy and imaging are not significantly biased by radiative transfer effects in typical infiltrates. However, more accurate estimates of cell properties including scattering and absorption cross-sections are needed to more accurately quantify these effects for specific microbes. Future work will focus on empirical characterization of absorption and scattering characteristics of well-known bacteria, combined with detailed modeling and experiments to evaluate the utility of quantitative fluorescence imaging and spectroscopy for biofilm characterization.

## CRediT authorship contribution statement

**Joshua M. Herzog:** Writing – review & editing, Writing – original draft, Visualization, Validation, Supervision, Conceptualization, Data curation, Formal analysis, Investigation, Methodology, Software. **Gianna Agosta:** Writing – original draft, Investigation, Visualization. **Volker Sick:** Supervision, Resources, Project administration, Funding acquisition, Writing – review & editing.

## Declaration of competing interest

The authors declare the following financial interests/personal relationships which may be considered as potential competing interests: Joshua M. Herzog and Volker Sick have a patent pending to The Regents of the University of Michigan. Gianna Agosta declares no known competing financial interests or personal relationships that could have appeared to influence the work reported in this paper.

## Data availability

Data will be made available on request.

## Appendix. Fluorescence intensity approximation

Assuming scattering effects are negligible, the fluorescence intensity can be derived analytically as follows. The $X$ and $Y$ functions are exactly

$$X = 1 \tag{A.1a}$$

and

$$Y = e^{-\frac{\tau}{\mu}} \tag{A.1b}$$

for cases in which scattering is negligible. This follows from the integral equations for $X$ and $Y$ where either $\tau \to 0$ or $\alpha \to 0$, *e.g.*, for strongly absorbing cases. From these functions, the moments are

$$x_0 = \frac{\alpha}{2}, \tag{A.2a}$$

$$x_1 = \frac{\alpha}{4}, \tag{A.2b}$$

$$y_0 = \frac{\alpha}{2}\left(\tau E_i(-\tau) + e^{-\tau}\right) = \frac{\alpha}{2}E_2(\tau), \tag{A.2c}$$

and

$$y_1 = \frac{\alpha}{2}\left(\frac{1-\tau}{2}e^{-\tau} - \frac{\tau^2}{2}E_i(-\tau)\right) = \frac{\alpha}{4}\left(1-\tau E_2(\tau)\right) \tag{A.2d}$$

where $E_i(z)$ is the exponential integral function and $E_n(z)$ is the generalized exponential integral ($E_i(z) = -E_1(-z)$). The amount of light absorbed per unit optical depth is given by the Beer–Lambert law

$$\frac{\partial A}{\partial \tau} = (1-\alpha)e^{-\tau} \tag{A.3}$$

assuming the incident direction is $\mu_0 = 1$. Integrating over the fluorescence intensity function results in, after simplification,

$$F = \Phi(1-\alpha)\frac{\alpha^2}{16}\left(1-e^{-2\tau}+\tau e^{-\tau}E_2(\tau)\right) = \Phi(1-\alpha)\frac{\alpha^2}{16}\left(1-2e^{-\tau}E_3(\tau)\right). \tag{A.4}$$

The fluorescence intensity is a separable function of $\alpha$ and $\tau$; the fluorescence intensity at any value of $\tau$ scales as

$$F \propto \Phi(1-\alpha)\alpha^2. \tag{A.5}$$

The fluorescence intensity described by Eq. (A.4) increases monotonically with $\tau$ which is expected. However, somewhat counter-intuitively, fluorescence intensity is not monotonic with effective albedo. Instead, the intensity peaks at $\alpha = 2/3$. For $g = 0.98$ as used in the simulation, the effective albedo is $2/3$ for $\alpha \approx 0.99$ which is consistent with the simulation results.

## References


[1] Rennie M, Lindvere-Teene L, Tapang K, Linden R. Point-of-care fluorescence imaging predicts the presence of pathogenic bacteria in wounds: a clinical study. J Wound Care 2017;26(8):452–60.

[2] Bachmann L, Zezell DM, Ribeiro AdC, Gomes L, Ito AS. Fluorescence spectroscopy of biological tissues—a review. Appl Spectrosc Rev 2006;41(6):575–90.

[3] Chinen AB, Guan CM, Ferrer JR, Barnaby SN, Merkel TJ, Mirkin CA. Nanoparticle probes for the detection of cancer biomarkers, cells, and tissues by fluorescence. Chem Rev 2015;115(19):10530–74.

[4] Zhang RR, Schroeder AB, Grudzinski JJ, Rosenthal EL, Warram JM, Pinchuk AN, et al. Beyond the margins: real-time detection of cancer using targeted fluorophores. Nat Rev Clin Oncol 2017;14(6):347–64.

[5] Herzog JM, Sick V. Quantitative spectroscopic characterization of near-UV/visible E. coli (pYAC4), B. subtilis (PY79), and green bread mold fungus fluorescence for diagnostic applications. J Fluorescence 2023;1–13.

[6] Ammor MS. Recent advances in the use of intrinsic fluorescence for bacterial identification and characterization. J Fluorescence 2007;17:455–9.

[7] Lee E-S, de Josselin de Jong E, Jung H-I, Kim B-I. Red fluorescence of dental biofilm as an indicator for assessing the efficacy of antimicrobials. J Biomed Opt 2018;23(1):015003.

[8] Jun W, Kim MS, Lee K, Millner P, Chao K. Assessment of bacterial biofilm on stainless steel by hyperspectral fluorescence imaging. Sens Instrum Food Qual Saf 2009;3:41–8.

[9] Carstea EM, Bridgeman J, Baker A, Reynolds DM. Fluorescence spectroscopy for wastewater monitoring: a review. Water Res 2016;95:205–19.

[10] Hanson RK, Spearrin RM, Goldenstein CS. Spectroscopy and optical diagnostics for gases, vol. 1, Springer; 2016.

[11] Ung L, Bispo PJ, Shanbhag SS, Gilmore MS, Chodosh J. The persistent dilemma of microbial keratitis: Global burden, diagnosis, and antimicrobial resistance. Surv Ophthalmol 2019;64(3):255–71.

[12] Herzog JM, Sick V. Design of a line-of-sight fluorescence-based imaging diagnostic for classification of microbe species. Meas Sci Technol 2023;34(9):095703.

[13] Herzog JM, Sick V. Fluorescence imaging for the anterior segment of the eye. Front Photonics 2024;4:1336541.

[14] Oelkrug D. Fluorescence spectroscopy in turbid media and tissues. In: Topics in fluorescence spectroscopy: probe design and chemical sensing. Springer; 2002, p. 223–53.

[15] Panigrahi SK, Mishra AK. Inner filter effect in fluorescence spectroscopy: As a problem and as a solution. J Photochem Photobiol C 2019;41:100318.

[16] Kühn H, Fredrich-Thornton ST, Kränkel C, Peters R, Petermann K. Model for the calculation of radiation trapping and description of the pinhole method. Opt Lett 2007;32(13):1908–10.

[17] Yu H, Qu F, Wu Z, He J, Rong H, Liang H. Front-face fluorescence excitation-emission matrix (FF-EEM) for direct analysis of flocculated suspension without sample preparation in coagulation-ultrafiltration for wastewater reclamation. Water Res 2020;187:116452.

[18] Zandomeneghi M, Carbonaro L, Caffarata C. Fluorescence of vegetable oils: olive oils. J Agricult Food Chem 2005;53(3):759–66.

[19] Hirsch RE. Front-face fluorescence spectroscopy of hemoglobins. Methods Enzymol 1994;232:231–46.

[20] Bevilacqua M, Rinnan Å, Lund MN. Investigating challenges with scattering and inner filter effects in front-face fluorescence by PARAFAC. J Chemometrics 2020;34(9):e3286.

[21] Wind L, Szymanski W. Quantification of scattering corrections to the Beer-Lambert law for transmittance measurements in turbid media. Meas Sci Technol 2002;13(3):270.

[22] Chandrasekhar S. Radiative transfer. 1st ed. New York: Dover Publications, Inc.; 1960, p. 1–393.

[23] Kubelka P, Munk F. An article on optics of paint layers. Z Tech Phys 1931;12(593–601):259–74.

[24] Myrick ML, Simcock MN, Baranowski M, Brooke H, Morgan SL, McCutcheon JN. The Kubelka-Munk diffuse reflectance formula revisited. Appl Spectrosc Rev 2011;46(2):140–65.

[25] Joseph RI, Thomas ME. How accurate is the Kubelka-Munk theory of diffuse reflection? A quantitative answer. In: Reflection, scattering, and diffraction from surfaces III, vol. 8495, SPIE; 2012, p. 132–40.

[26] Jacques SL. Monte Carlo modeling of light transport in tissue (steady state and time of flight). In: Optical-thermal response of laser-irradiated tissue. Springer; 2010, p. 109–44.

[27] Zhu C, Liu Q. Review of Monte Carlo modeling of light transport in tissues. J Biomed Opt 2013;18(5):050902.

[28] Balaev AE, Dvoretski K, Doubrovski VA. Refractive index of escherichia coli cells. In: Saratov fall meeting 2001: optical technologies in biophysics and medicine III, vol. 4707. SPIE; 2002, p. 253–60.

[29] Bryant FD, Seiber B, Latimer P. Absolute optical cross sections of cells and chloroplasts. Arch Biochem Biophys 1969;135:97–108.

[30] Konstantopoulos A, Kuo J, Anderson D, Hossain P. Assessment of the use of anterior segment optical coherence tomography in microbial keratitis. Am J Ophthalmol 2008;146(4):534–42.

[31] Henyey LG, Greenstein JL. Diffuse radiation in the galaxy. Astrophys J 1941;93:70–83.

[32] Wehrse R, Kalkofen W. Advances in radiative transfer. Astron Astrophys Rev 2006;13:3–29.

[33] Van de Hulst H, Graaff R. Aspects of similarity in tissue optics with strong forward scattering. Phys Med Biol 1996;41(11):2519.

[34] Van de Hulst H, Kattawar GW. Exact spread function for a pulsed collimated beam in a medium with small-angle scattering. Appl Opt 1994;33(24):5820–9.

[35] Scott TG, Spencer RD, Leonard NJ, Weber G. Emission properties of NADH. Studies of fluorescence lifetimes and quantum efficiencies of NADH, AcPyADH, and simplified synthetic models. J Am Chem Soc 1970;92(3):687–95.